Noise correction of turbulent spectra obtained from Acoustic Doppler Velocimeters

Vibhav Durgesh[a], Jim Thomson[b], Marshall C. Richmond[a,*], Brian L. Polagye[b]

[a] *Hydrology Group, Pacific Northwest National Laboratory, Richland, WA 99352*
[b] *Northwest National Marine Renewable Energy Center, University of Washington, Seattle, WA 98105*

Abstract

Turbulent Kinetic Energy (TKE) frequency spectra are essential in characterizing turbulent flows. The Acoustic Doppler Velocimeter (ADV) provides three-dimensional time series data at a single point in space which are used for calculating velocity spectra. However, ADV data are susceptible to contamination from various sources, including instrument noise, which is the intrinsic limit to the accuracy of acoustic Doppler processing. This contamination results in a flattening of the velocity spectra at high frequencies ($\mathcal{O}(10)$Hz). This paper demonstrates two elementary methods for attenuating instrument noise and improving velocity spectra. First, a "Noise Auto-Correlation" (NAC) approach utilizes the correlation and spectral properties of instrument noise to identify and attenuate the noise in the spectra. Second, a Proper Orthogonal Decomposition (POD) approach utilizes a modal decomposition of the data and attenuates the instrument noise by neglecting the higher-order modes in a time-series reconstruction. The methods are applied to ADV data collected in a tidal channel with maximum horizontal mean currents up to 2 m/s. The spectra estimated using both approaches exhibit an $f^{-5/3}$ slope, consistent with a turbulent inertial sub-range, over a wider frequency range than the raw spectra. In contrast, a Gaussian filter approach yields spectra with a sharp decrease at high frequencies. In an example application, the extended inertial sub-range from the NAC method increased the confidence in estimating the turbulent dissipation rate, which requires fitting the amplitude of the $f^{-5/3}$ region. The resulting dissipation rates have smaller uncertainties and are more consistent with an assumed local balance to shear production, especially for mean horizontal currents less than 0.8 m/s.

Keywords: Marine-Hydro Kinetic (MHK) devices, Turbulent flow, Turbulent Kinetic Energy (TKE) Spectra, ADV, Doppler /instrument Noise

1. Introduction

Acoustic Doppler Velocimeter (ADV) data are commonly used for performing field measurements in rivers and oceans [1, 2, 3, 4, 5]. The ADV measures fluid velocity by comparing the Doppler phase shift

*E-mail: marshall.richmond@pnl.gov

of coherent acoustic pulses along three axes, which are then transformed to horizontal and vertical components. In contrast to an an Acoustic Doppler Current Profiler (ADCP), the ADV samples rapidly ($\mathcal{O}(10)$ Hz) from a single small sampling volume ($\mathcal{O}(10^{-2})$m diameter). The rapid sampling is useful for estimating the turbulent intensity, Reynolds stresses, and velocity spectra. Velocity spectra are useful in characterizing fluid flow and are also used as an input specification for synthetic turbulence generators (e.g, TurbSim [6] and computational fluid dynamics (CFD) simulations (viz. TrubSim). These simulations require inflow turbulence conditions for calculations of dynamic forces acting on Marine and Hydro-Kinetic (MHK) energy conversion devices [see 7]. This study focuses on accurate estimation of velocity spectra from ADV measurements that are contaminated with noise, for application in CFD simulations for MHK devices.

ADV measurements are contaminated by Doppler noise, which is the intrinsic limit in determining a unique Doppler shift from finite length pulses [8, 9, 10]. Doppler noise, also called "instrument noise", can introduce significant error in the calculated statistical parameters and spectra. Several previous papers have addressed Doppler noise and its effect on the calculated spectra and statistical parameters [5, 8, 9, 10]. These studies have shown that the Doppler noise has properties similar to that of white noise and is associated with a spurious flattening of ADV spectra at high frequencies [8, 9]. In the absence of noise, velocity spectra in the range of 1 to 100 Hz are expected to exhibit an $f^{-5/3}$ slope, termed the inertial sub-range [11, 12, 13]. Nikora et.al. [8] showed that the spurious flattening at high frequencies is significantly greater for the horizontal u and v components of velocity as compared to the vertical w component of velocity, and is a result of the ADV beam geometry. Motivated by the many applications of velocity spectra, this study examines the effectiveness of two elementary techniques to minimize the contamination by noise in velocity spectra calculated from ADV data.

ADV measurements are also contaminated by spikes, which are random outliers that can occur due to interference of previous pulses reflected from the flow boundaries or due to the presence of bubbles, sediments, etc in the flow. Several previous papers have demonstrated methods to identify, remove and replace spikes in ADV data [14, 15, 16, 17, 18]. For example, Elgar and Raubenheimer[14], and Elgar et. al. [16] have used the backscattered acoustic signal strength and correlation of successive pings to identify spikes. Once the spike has been identified, it can be replaced with the running average without significantly influencing statistical quantities [18]. Another technique that is commonly used to de-spike ADV data is Phase-Space-Thresholding (PST) [19]. This technique is based on the premise that the first and second derivatives of the turbulent velocity component form an ellipsoid in 3D phase space. This ellipsoid is projected into 2D space and data points located outside a previously determined threshold are identified as spikes and eliminated. The PST approach is an iterative procedure wherein iterations are stopped when no new spikes can be identified. There are several variations of this approach, such as 3D-PST and PST-L, detailed descriptions of which are given in [15, 17]. In the present study, an existing method for despiking from [16] is applied, and we restrict our investigation to Doppler noise.

One existing technique to remove Doppler noise from ADV data is a low-pass Gaussian digital filter [10, 20, 21, 22, 23]. Although this technique is capable of eliminating Doppler noise from the total variance, the spectra calculated from filtered data exhibit a sharp decrease at high frequencies. In contrast, Hurther and Lemmin [24], using a four beam Doppler system, estimated the noise spectrum from cross-spectra evaluations of two independent and simultaneous measurements of the same vertical velocity component. After the correction, spectra obtained by Hurther and Lemmin [24] exhibit an $f^{-5/3}$ slope out to the highest frequency (Nyquist frequency).

The present study explores two different approaches for attenuating noise and thereby improving velocity spectra at high frequencies. The first approach, termed the "Noise Auto-Correlation" (NAC) approach, utilizes assumed spectral and correlation properties of the noise to subtract noise from the velocity spectra. The NAC approach is analogous to the Hurther and Lemmin [24] approach, but differs in that they estimate the noise variance using the difference between two independent measures of vertical velocity, whereas in this study the noise variance is estimated from the flattening of the raw velocity spectra. The second approach uses Proper Orthogonal Decomposition (POD) to decompose the velocity data in a series of modes. In POD, the maximum possible fraction of TKE is captured for a projection onto a given number of modes. Combinations of POD modes identify the energetic structures in turbulent data fields [25, 26, 27, 28, 29]. Low-order reconstructions of the ADV data are performed using a reduced number of POD modes which are associated only with the energetic structures in the turbulent flows. This eliminates the random and less energetic fluctuations associated with instrument noise.

The field measurements and raw velocity spectra are described in §2 and the methods to attenuate noise from velocity spectra follow in §3. Before detailing the NAC and POD approaches (§3.1 & §3.2, respectively), the assumptions implicit to both methods are described in §32.1. Results, in the form of noise-corrected spectra from both methods, are presented in §4. The noise-corrected spectra are compared with spectra from a Gaussian filter approach in §4.3 and evaluated for theoretical isotropy in §4.4. Finally, an example application is given in §5, where the NAC method is used to reduce uncertainties in estimating the turbulent dissipation rates from the field dataset, especially during weak tidal flows. The NAC method estimates of dissipation rates are also more consistent with an assumed TKE budget, wherein shear production balances dissipation. Conclusions are stated in §6.

2. Field measurements

ADV measurements were collected in Puget Sound, WA (USA) using a 6-MHz Nortek Vector ADV. The site is near Nodule Point on Marrowstone Island at $48^o\ 01'55.154''$ N $122^o39'40.326''$ W and 22 m water depth, as shown in Fig. 1. The ADV was mounted on a tripod that was 4.6 m above the sea bed (the intended hub height for a tidal energy turbine), and it acquired continuous data at a sampling frequency f_s

Figure 1: Regional map, bathymetry, and location of ADV measurements at Marrowstone Island site in Puget Sound, northwest of Seattle, WA.

of 32 Hz for four and a-half days during spring tide in February 2011. The mean horizontal currents ranged from 0 to 2 m/s. The measurement location was sufficiently deep (17 m below the water surface at mean lower low water) where the influence of wave orbital velocities may be neglected. The measurement location is in close proximity to headlands, which can cause flow separation and produce large eddies, depending on the balance of tidal advection, bottom friction, and local acceleration due to the headland geometry. In a prior deployment at the same location, the tripod was instrumented with a HOBO Pendant-G for collecting acceleration data. Results indicate that tripod motion (e.g., strumming at the natural frequency) is unlikely to bias measurements. For further details about the measurement site location and data, see [5, 30].

The raw data acquired from the ADV are shown in Fig. 2(a), where a few spikes are obvious in the raw data. The flow velocity did not exceed the preset velocity range of the ADV [see 5, 30], and there was no contamination from the flow boundary (ADV was positioned facing upward). Thus, these are treated as spikes and removed according to Elgar and Raubenheimer [14], and Elgar et al. [16]. The spikes constitute less than 1% of all data, thus a more advanced algorithm was not necessary. Before performing this Quality Control (QC), the continuous data are broken into sets of 300 s (five minutes) data records, each containing 9600 data points, which yields 1256 independent data records. This ensures that the velocity measurements are stationary (i.e., stable mean and variance) for each set, which is essential for implementing a de-spiking approach, calculating statistical quantities, and calculating velocity spectra [31]. Furthermore, two-sample Kolmogorov-Smirnov test is performed to validate that the samples for a given record have the same distribution with a 5% significance level. The QC routine removes data with low pulse-to-pulse correlations, which are associated with spikes in the ADV data. A low correlation cut-off c value [14, 16] is determined using the equation $c = 30 + 40\sqrt{f_s/f_{max}}$ where f_s is the actual sampling frequency and f_{max} is the maximum possible sampling frequency. The average acoustic correlations for the ADV measurements performed for this investigation are 93.35, 96.70 and 96.72 for beam-1, beam-2, and beam-3 respectively, while the minimum values of the average acoustic correlations are 88.85, 93.62 and 93.42 for beam-1, beam-2, and beam-3 respectively. The number of spurious points is less than 1% of the total points, and these spurious data points are replaced with the running mean. It has been shown that interpolation of data along the small gaps between data points that have been replaced by the running mean does not significantly alter the spectra or the second order moments, provided only a few data points are replaced [14, 16, 18]. The approach used here successfully eliminates the obvious spikes from the entire raw data, as shown in Fig. 2(b). The ADV data set from which spikes have been removed will be referred to as QC ADV data in the remainder of the paper.

2.1. Flow Scales

The ADV data were collected in an energetic tidal channel with a well-developed bottom boundary layer (BBL). In such a boundary layer, the canonical expectation is for a turbulent cascade to occur which transfers energy from the large scale eddies (limited by the depth or the stratification) to the small scale eddies (limited by viscosity). In frequency, this cascade occurs in the $f^{-5/3}$ inertial sub-range, assuming advection of a frozen field (i.e., Taylor's hypothesis $f = \langle u \rangle / L$). The extent of this frequency range can be estimated from the energetics of the flow. Independent estimates of the turbulent dissipation rates ϵ (using the structure function of collocated ADCP data, see [5, 32, 33]) range from 10^{-6} to 10^{-4} m^2/s^3. The Kolmovgorov scale, at which viscosity ν acts and limits the inertial sub-range, is given by $L_k = (\nu^3/\epsilon)^{1/4}$, and thus ranges from 10^{-3} to 10^{-4} m. Converting this length scale to frequency by advection of a mean flow of $\mathcal{O}(1)$ m/s, we expect the inertial sub-range will extend to a frequency of 10^3 to 10^4 Hz. This is well beyond the 16 Hz maximum (i.e., Nyquist frequency) of the following analysis, and thus we expect the true spectra to follow a $f^{-5/3}$ slope throughout the higher frequencies.

Another consideration for the high frequency spectra is the sampling volume of the measurement. Using the 0.014 m diameter sampling volume setting in the Nortek configuration software, the corresponding maximum frequency for accurate measurements is $f = \langle u \rangle / L = 1/0.014 = 71$ Hz, which is again greater than the 16 Hz maximum (i.e., Nyquist frequency) of the following analysis. At lower speeds this frequency will decrease (and vice-versa), and at 0.22 m/s the frequency becomes equal to the 16 Hz Nyquist frequency of our data. Thus, the sampling volume is sufficiently small for accurate high-frequency measurements in all but the weakest tidal conditions (horizontal mean currents less than 0.22 m/s occur for only 6% of the dataset).

The lowest frequency of the inertial sub-range is set by the size of the large energy-containing eddies, and for isotropy, these must be smaller than the distance to the boundary (4.6 m) or the Ozimdov length. Since the site is well-mixed, the distance to the boundary is the limiting scale, and, again using Taylor's frozen turbulence hypothesis, suggests that the lower bound for the inertial sub-range is ∼0.2 Hz. Thus, we expect, from dynamical arguments alone, to observe isotropic $f^{-5/3}$ spectra from approximately 10^{-1} to 10^{4} Hz, and deviations in the spectra from the $f^{-5/3}$ slope in this range suggest noise contamination in the ADV data.

2.2. Spectra

The observed TKE varied significantly during each tidal cycle, and the 1256 records of QC ADV data are divided into two groups: slack and non-slack tidal conditions. The slack tidal and non-slack tidal conditions are the time periods when the mean horizontal velocity magnitudes for a record are less than and greater than 0.8 m/s respectively [5, 30]. This cutoff is chosen primarily for relevance to tidal energy turbines, which typically begin to extract power at $\mathcal{O}(1)$ m/s. However, the 0.8 m/s criterion is also relevant to the conditions for which noise creates uncertainty in the turbulent dissipation rate (see §5).

There are 525 data records of slack tidal condition and 731 data records of non-slack tidal condition, with each record containing 300 s of data and 9600 data points. The energy spectra of the u, v, and w velocity components are calculated for each ADV data record using the Fast Fourier Transform (FFT) algorithm on Hamming-tapered windows of 1024-points each with 50% overlap. This yields approximately 47 equivalent Degrees of Freedom (DOF) [34]. The mean velocity spectra for the non-slack and slack tidal conditions are shown in Figs. 3(a) and (b) respectively. The energy in the spectra decreases with increasing frequency, with a flat noise-floor at high frequencies. The mean spectra for all components of velocity are similar, suggesting a quasi-isotropic turbulence, except at high frequencies, where the noise-floor is lower in the vertical velocity spectra than in the horizontal velocity spectra. This difference in noise is a well-known consequence of the ADV beam alignment (30 deg from vertical, 60 deg from horizontal) [9, 35].

As shown in Figs. 4(a)-(c) for slack and non-slack tidal conditions, the grey lines represent the spectra associated with each QC ADV data record, and the solid and dash red, green and blue lines represent the ensemble-averaged spectra for u, v and w components of velocity for slack and non-slack tidal conditions

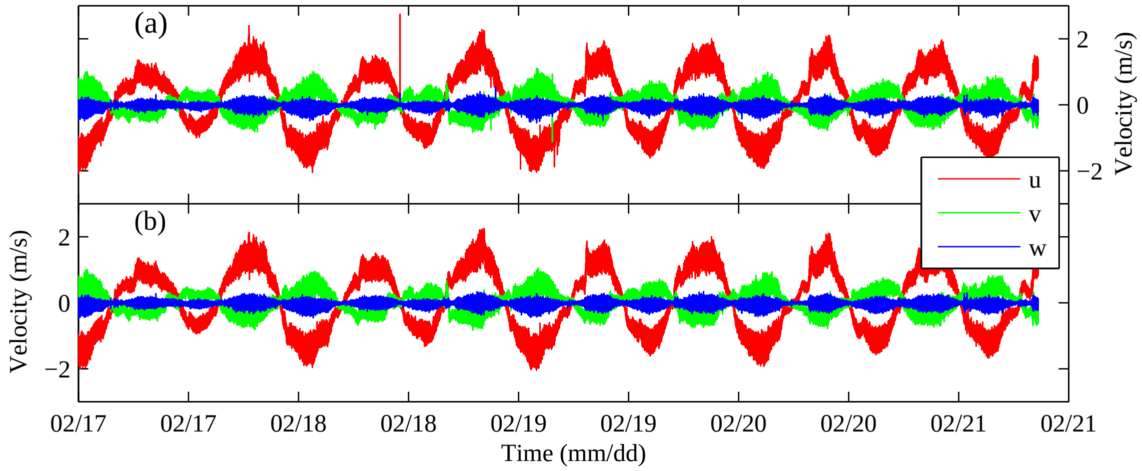

Figure 2: Data from ADV: (a) raw velocity data, and (b) velocity data after QC step.

respectively. The spectra for the individual records exhibit significant fluctuations from one record to the next, suggesting that there is a significant change in TKE even for the non-slack tidal condition. The ensemble-averaged spectra shown in these figures have a $f^{-5/3}$ slope in the inertial sub-range [11, 12, 13, 36], which is typical for turbulent flows, and indicative of classic Kolmogorov cascade of energies from the larger to smaller scale eddies. As discussed in §2.1, inertial sub-range should extend from the frequency range of $\mathcal{O}(10^{-1})$ Hz to $\mathcal{O}(10^{4})$ Hz. However, it is observed from these figures that the ensemble-averaged spectra for u and v components of velocity display a flattening at frequencies greater than 1 Hz for horizontal components (i.e., a deviation from $f^{-5/3}$ slope in inertial sub-range). This is consistent with the effect of instrument noise observed by Nikora and Goring [8], and Voulgaris and Trowbridge [9]. Nikora and Goring [8] defined a characteristic frequency (f_b), which separates two regions in the spectra: 1) the region where TKE is much larger than the instrument noise energy (i.e., for $f \leq f_b$) and 2) the region where TKE is comparable to the instrument noise energy (i.e., for $f \geq f_b$). The flattening of the spectra is always observed in the region of comparable turbulence and instrument noise energies (i.e., for the region in spectra with $f \geq f_b$). For this study, the characteristic frequencies for non-slack and slack tidal conditions, for both u and v spectra, are observed to be approximately 2.5 Hz and 1.0 Hz, respectively. For vertical spectra, the flattening associated with noise is only evident during slack conditions; however, this is still sufficient to degrade estimates of the turbulent dissipation (see §5).

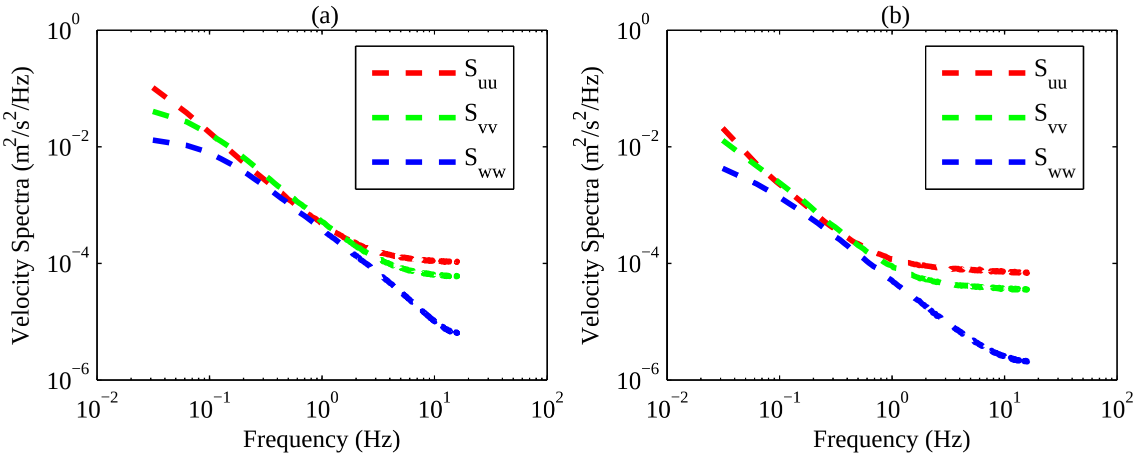

Figure 3: Mean velocity spectra of QC ADV data for u, v, and w components:(a) non-slack tidal condition and (b) slack tidal condition.

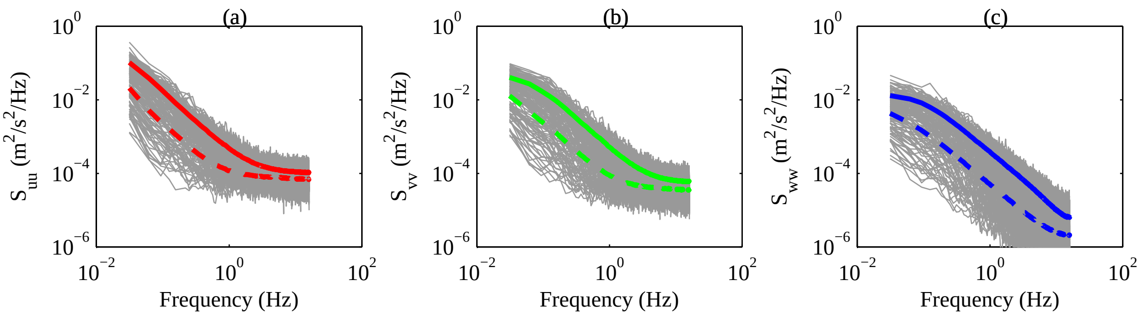

Figure 4: Ensemble-averaged spectra for the non-slack (solid colors) and slack (dashed colors) tidal conditions: (a)-(c), u, v, and w components of velocity respectively. Grey lines represent the spectra calculated from individual data records of 300 s each.

3. Methods

3.1. "Noise Auto-Correlation" (NAC)

Studies by Nikora and Goring [8], Voulgaris and Trowbridge [9], and Garcia et al. (2005) [10] have shown that ADV noise is well approximated as Gaussian white noise. They have also shown that the presence of instrument noise in the spectra is associated with flattening of spectra at higher frequencies. The following "Noise Auto-Correlation" (NAC) approach exploits the properties of white noise to identify and attenuate the contribution of instrument noise from the spectra. Although elementary in theory, this classic treatment of noise is appealing because it is simple, direct, and computationally efficient. More advanced techniques, which might treat any nonlinear effects and relax the assumptions on the noise, may be required for other applications.

First, the time series ($x(t)$) is assumed to be contaminated with white noise, and is expressed as the summation of the true signal ($x_s(t)$) and white noise ($wn(t)$),

$$x(t) = x_s(t) + wn(t), \tag{1}$$

where t is time. The auto-correlation ($R_{x,x}(\tau)$) calculated of the data is

$$R_{x,x}(\tau) = E[x(t)x(t+\tau)], \tag{2}$$

where E represents the expected value, t is time, and τ represents the time-lag associated with auto-correlation. The auto-correlation given by Eq. 2 can also be expressed as the summation of auto-correlations (i.e., R_{x_s,x_s} and $R_{wn,wn}$) and cross-correlations (i.e., $R_{x_s,wn}$ and R_{wn,x_s}) of the true signal and white noise [37, 38],

$$R_{x,x}(\tau) = R_{x_s,x_s}(\tau) + R_{wn,wn}(\tau) + \underbrace{R_{x_s,wn}(\tau)}_{0} + \underbrace{R_{wn,x_s}(\tau)}_{0}. \tag{3}$$

In Eq. 3, it should be noted that the cross-correlation between true signal and white noise will approach zero for long time series [37, 38]. Therefore, $R_{x,x}$ is expressed as the summation of auto-correlation of true signal and white noise only, as shown in Eq. 3. The auto-correlation function of white noise is a delta function with magnitude equal to the total variance of the white noise (i.e., B) at zero time-lag. Therefore, it is expected that the auto-correlation function of a signal contaminated with white noise would exhibit a spike at zero time-lag, since $R_{x,x}(\tau)$ is the summation of the auto-correlation of clean signal and white noise, schematic of which is shown in the Figs. 5(a)-(c).

Similarly, the spectrum ($S_{x,x}(f)$) calculated from the contaminated data can also be expressed as the summation of the true spectrum ($S_{x_s,x_s}(f)$) and the noise spectrum ($S_{wn,wn}(f)$),

$$S_{x,x}(f) = S_{x_s,x_s}(f) + S_{wn,wn}(f), \tag{4}$$

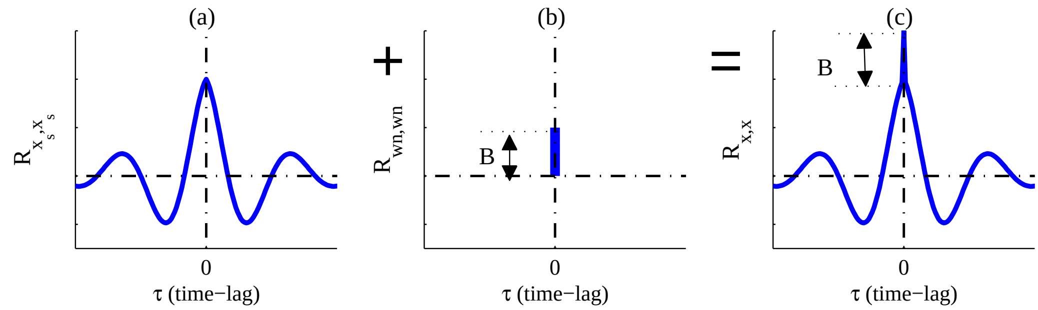

Figure 5: Schematic showing the effect of white noise contamination in the auto-correlation function: (a) schematic of auto-correlation function of clean signal, (b) schematic of auto-correlation function of white noise, and (c) schematic of auto-correlation function of clean signal with white noise.

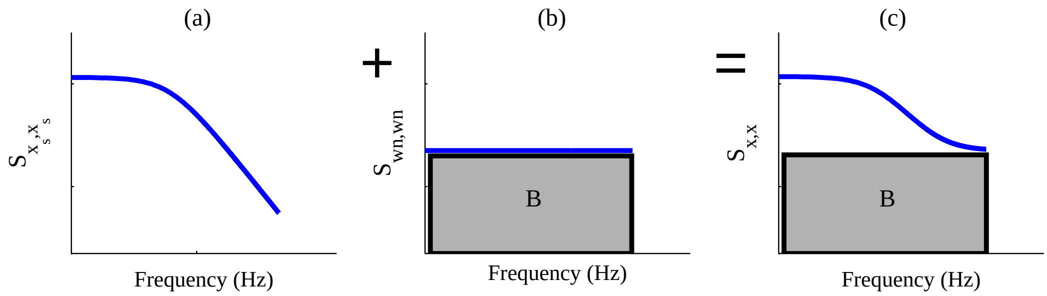

Figure 6: Schematic showing the effect of white noise contamination in the auto-spectral density function: (a) schematic of auto-spectral density function of clean signal, (b) schematic of auto-spectral density function of white noise, and (c) schematic of auto-spectral density function of clean signal with white noise.

where f is the frequency in Hz. The spectrum of the white noise acquires a constant value at all frequencies and the total energy in the white noise (i.e., B) is the area under the spectrum, as shown in Fig. 6 (b). At higher frequencies, where the spectrum of clean signal has energy comparable to the spectrum of white noise, the spectrum of contaminated signal is expected to flatten out, as schematically shown in Figs. 6(a)-(c). Nikora and Goring [8] in their study have suggested that the flattening of the spectra is always observed in the frequency with comparable spectral energies of clean signal and instrument noise. Furthermore, they have also estimated the energy contribution of instrument noise (i.e., B) by calculating the area of the rectangular region extending over all frequencies, with energy levels equal to those of the flattened portion of the spectrum [8, 10].

If the energy contribution from the white noise (i.e., B) is known, the auto-correlation function of the clean signal (i.e., $R_{x_s,x_s}(\tau)$) can be estimated using the following sets of equations

$$R_{wn,wn}(\tau) = \begin{cases} B & \text{if } \tau = 0; \\ 0 & \text{otherwise.} \end{cases} \tag{5}$$

$$R_{x_s,x_s}(\tau) = R_{x,x}(\tau) - R_{wn,wn}(\tau). \tag{6}$$

Finally, the spectra ($S_{x_sx_s}(f)$) of the clean data can be estimated by Fourier transforming the auto-correlation of the true signal determined using Eq. 6, given as

$$S_{x_sx_s}(f) = \int_{-\infty}^{\infty} R_{x_s,x_s}(\tau) e^{-i2\pi f\tau} d\tau. \tag{7}$$

Here, the NAC approach requires estimating the energy contribution of instrument noise (i.e., B) from the raw spectra, and then using Eqs. 5 and 6 to obtain the auto-correlation function of the noise-removed data. An independent *a priori* estimate of the noise variance would be preferable; however, that is not possible for a pulse coherent Doppler system, because the noise depends on the correlations of all the pulse pairs (i.e., it is not expected to be constant across all conditions or data records). After determining B, one can calculate the Fourier transform of the noise-removed auto-correlation function to estimate the noise-corrected spectra. Again, it should be noted that the NAC approach is only capable of attenuating the instrument noise from the spectra because instrument noise is assumed to be white noise. Unlike the POD method in the following section, the NAC approach can only estimate noise-corrected frequency spectra, and not noise-corrected time series data.

3.2. Proper Orthogonal Decomposition (POD)

Proper Orthogonal Decomposition (POD) has been used in fluid dynamics for at least 40 years (Lumley [25]). Singular System Analysis, Karhunen-Loeve decomposition, Principle Component Analysis [39], and Singular Value Decomposition (SVD), are names of POD implementations in other disciplines [see 26]. POD is a robust, unambiguous technique, and when applied to a turbulent flow field data set, it can identify dominant features or structures in the data set. Decomposition of the turbulent flow field data by this technique provides a set of modes, and the combination of these modes can be used to represent flow structures containing most of the energy. Moreover, these POD modes are orthogonal and optimal, thus, they provide a compact representation of structures in the flow. POD has been used to study axisymmetric jets [27, 28], shear layer flows [40], axisymmetric wakes [41], coherent structures in turbulent flows [42], and, in the field of wind energy by [43]. Here, POD is used to identify and attenuate noise from the ADV data by performing a low-order reconstruction of the ADV data using only selective, low-order POD modes.

When applied to the turbulent velocity data set, the POD technique yields a set of optimal basis functions or POD modes (ϕ's). These POD modes are optimal in the sense that they maximize the projection of the turbulent data sets on to the POD modes in a mean square sense, expressed as [see 25, 26]

$$\frac{\langle |(u,\phi)|^2 \rangle}{\|\phi\|^2}, \tag{8}$$

where $\langle . \rangle$ is the average operator, $(.,.)$ represents the inner product, $|.|$ represents the modulus, and $\|.\|$ is the L^2-norm. Maximization of $\langle |(u, \phi)|^2 \rangle$ when subjected to the constraint $\|\phi\|^2 = 1$, leads to an integral eigenvalue problem given as [for detailed derivation see 25, 26]

$$\int_{\Omega} \langle \mathrm{u}(t) \otimes \mathrm{u}(t') \rangle \phi dt = \lambda \phi(t), \tag{9}$$

where Ω is the domain of interest, u is the velocity field (can be either vector or scalar quantities), $\otimes$ is the tensor product, $\langle \mathrm{u}(t) \otimes \mathrm{u}(t') \rangle$ is the ensemble-averaged autocorrelation tensor of the velocity records forming the kernel of the POD, and λ is the energy associated with each POD mode.

After discretization of Eq. 9, the matrix formulation of the POD implementation for a turbulent data field [see 44, 45, 46] is given by

$$[\mathbb{R}_{uu}]\{\phi\} = \lambda\{\phi\}, \tag{10}$$

where $\mathbb{R}_{uu}$ is the ensemble-averaged correlation tensor matrix, ϕ is the POD mode, and λ is the energy captured by each POD mode. The correlation matrix calculated from the turbulent data set is also referred to as the POD kernel. For the POD implementation used in this study, ADV data were broken into 64 s records each containing 2048 data points, which yielded 2478 and 3410 data records for the slack and non-slack tidal conditions respectively. This is in contrast to the 300 s records used for the NAC method, and is necessary to constrain the size of the kernel matrix and thus the computational time. The resulting POD kernel matrix for each record is 2048 $\times$ 2048, yielding 2048 ϕ's and λ's. The slack and non-slack tidal conditions are defined as less than or greater than a horizontal mean flow of 0.8 m/s respectively.

Once determined, these POD modes can be used to reconstruct each velocity component as

$$\mathrm{u}^n(t) = \sum_{p=1}^{N} a_p^n \phi_p, \tag{11}$$

where $\mathrm{u}^n(t)$ is the n^{th} velocity data record, a_p^n is the time-varying coefficient for the pth POD mode and the n^{th} velocity data record, and N represents number of modes used for reconstructions. If all the POD modes (i.e., $N = 2048$ for this study) are used in the velocity field reconstruction, it should yield the original velocity data set or record. However, when a limited number of POD modes are used (i.e., $N < 2048$), the reconstructed velocity field is referred to as a low-order reconstruction. The time-varying POD coefficients (a_p) are obtained by projecting the velocity data field from each record onto the POD modes. For this study, there are 3140 and 2478 time varying coefficients associated with each POD mode for non-slack and slack tidal conditions respectively. The relevance of these POD modes (ϕ_p) in representing the coherent or energetic structures can be ascertained by analyzing the energy captured by each of these modes (i.e., λ_p) and also by analyzing the time-varying coefficients associated with these modes.

Since these POD modes are optimal and orthogonal,

$$(\phi_i, \phi_j) = \delta_{ij}, \tag{12}$$

$$\langle a_i a_j^* \rangle = \delta_{ij} \lambda_i, \tag{13}$$

where δ_{ij} is the Kronecker delta, a_j^* is the conjugate of a_j, $\langle\rangle$ ensemble-averaging, and (.) represents the inner product. These relationships are used for the verification of POD results.

When applied to a turbulent data set, the POD modes can be analyzed to identify the modes that are associated with non-coherent, low-energy, high frequency fluctuations in the flow field. Since the instrument noise is assumed to be white noise, it is expected that the contribution from the instrument noise will be non-coherent and will have low energy. Therefore, in a low-order reconstruction, the modes associated with noise are excluded. Similarly, Singular Spectrum Analysis (SSA) [47] is used to obtain information about the signal to noise separation when the noise is uncorrelated in time (i.e., white noise) in analysis of climatic time series. Durgesh et al. [42] demonstrated the ability of POD to filter small scale fluctuations in a swirling jet and turbulent wake, and capture coherent structures by performing low-order reconstructions.

4. Results

4.1. NAC implementation

The NAC method described in section 3 is implemented on the QC ADV data to correct for instrument noise. The results presented here will focus on the non-slack tidal condition (i.e., data records with the mean horizontal velocity magnitude greater than 0.8 m/s), since these are of greater operational interest for tidal energy turbines. However, the application in §5 emphasizes the slack conditions.

The first step in this approach is to estimate the noise variance, B, from the raw spectra [8]. At frequencies greater than a characteristic frequency (f_b), flattening of the spectra is observed, as shown in Figs. 4(a) and (b). At these frequencies, the spectra are dominated by instrument noise; therefore, the flattened portion of the spectra represents the energy level (or variance) contributed by instrument noise [8, 10]. The area of the rectangular region extending over all frequencies, with energy levels equal to those of the flattened portion of the spectra, can provide an estimate of total energy from instrument noise, since it exhibits behavior similar to that of Gaussian white noise [8]. A schematic representing the total contribution from instrument noise for a single component of velocity is shown in Fig. 6, the same approach is also used to calculate instrument noise contribution for v and w components of velocity. This approach has also been used by Nikora and Goring [8], Garcia et al. [10], Romagnoli et. al. [48] to estimate the contribution of instrument noise (Doppler noise) in ADV data. Here, to obtain an accurate estimate of the energy in the instrument noise, the mean energy value of the spectra from 12-16 Hz is used.

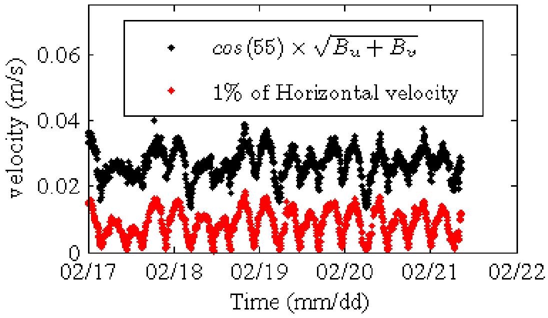

Figure 7: Estimated along-beam noise $n = \cos(55°)\sqrt{B_{uu} + B_{vv}}$ (black dots) and *a priori* noise value as n = 1% of the horizontal mean flow (red).

The average noise energies (variances) obtained are $B_{uu} \sim 0.0017 m^2/s^2$ and $B_{vv} \sim 0.0010 m^2/s^2$ for the u and v horizontal components of velocity, respectively. The corresponding horizontal error velocity is $\sqrt{B_{uu} + B_{vv}}$, which is converted to along beam error with cos(55°) and shown in Fig. 7 with the *a priori* 0.1% error velocity. The values and qualitative dependence on the mean flow speed are similar to [8].

The second step in the NAC approach is to calculate the auto-correlation of the true signal (i.e., $R_{uu,NAC}$ and $R_{vv,NAC}$) by subtracting the contribution of instrument noise from the auto-correlation values (i.e., R_{uu}, and R_{vv}),

$$R_{uu,NAC}(\tau) = \begin{cases} R_{uu}(\tau) - B, & \text{if } \tau = 0; \\ R_{uu}(\tau), & \text{otherwise,} \end{cases} \tag{14}$$

where B is the total energy or variance from the instrument noise.

The ensemble-averaged R_{uu}, R_{vv}, and R_{ww} as a function of time-lag (τ), for non-slack tidal condition, are shown in Fig. 8. As observed in the figure, the auto-correlation values approach zero with increase in τ, which is as expected for turbulent flows. Figures 9(a) and (b) show the mean R_{uu} and R_{vv} close to zero τ. As observed in the figures, the auto-correlations (i.e., R_{uu} and R_{vv}) show a spike or jump in value at zero τ, while R_{ww} shows a correlation curve without presence of a spike, as observed in Fig. 9(c). A spike in auto-correlation at zero τ is consistent with contamination by Gaussian white noise (see Eq. 3, 6, and Fig. 5).

$R_{uu,NAC}$ and $R_{vv,NAC}$ are estimated using Eq. 14, and are shown in Figs. 9(a) and (b) respectively. As observed in the figures, the spike in auto-correlation at zero time-lag is reduced after removing the estimated contribution of instrument noise (B). These corrected auto-correlation values are then used to calculate spectra (i.e., $S_{uu,NAC}$ and $S_{vv,NAC}$) using Eq. 7. The ensemble-averaged NAC spectra for u and v components of velocity, for the non-slack tidal condition, are shown in Figs. 10(a) and (b) respectively. As observed in these figures, there is more than an order of magnitude reduction in instrument noise level for both components of horizontal velocity at frequencies above f_b. Furthermore, the spectra exhibit an extended

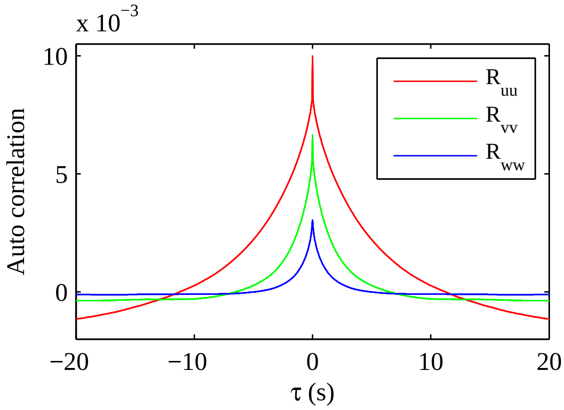

Figure 8: Ensemble-averaged auto-correlation for non-slack tidal condition from QC ADV data for all components of velocity R_{uu}, R_{vv}, and R_{ww}.

$f^{-5/3}$ inertial sub-range. The mean square error (MSE) of the corrected spectra from the expected $f^{-5/3}$ slope is calculated, and is shown in Fig. 11. As observed in the figure, there is significant decrease in the MSE value for NAC spectra compared with the MSE value obtained for raw spectra. A similar behavior is also observed for the slack tidal condition, as shown in Fig. 12. It should also be noted that NAC spectra from each 300 s record still exhibit significant variability, similar to the raw spectra, and ensemble averaging of several spectra is required to obtain smooth spectra.

A recent study done by Romagnoli et. al. [48] used a similar approach to estimate Doppler noise, and then used the energy in the Doppler noise to obtain corrected auto-correlation function and accurately estimate integral time length scales. However, the focus of this study is to obtain an accurate estimate of the velocity spectra for the purpose of CFD simulations. Therefore, in this work, the estimated energy in the Doppler noise was used to correct the auto-correlation function, and then the Fourier transform of the corrected auto-correlation function was used to obtain an accurate estimation of the velocity spectra.

4.2. POD implementation

The POD method is used to identify and attenuate the contribution of instrument noise from the QC ADV data and provide a comparison with the results obtained by NAC method since no direct observations of the true spectra at higher frequencies are available. The POD analysis is performed separately for u and v components of velocity during non-slack and slack tidal conditions. The detailed implementation and results for the non-slack condition, and certain relevant results for the slack tidal condition, are presented here.

For both components of horizontal velocity, POD modes and the energy in them are determined using the discretized POD equation, given in Eq. 10. The first six POD modes (dimensionless basis functions) obtained

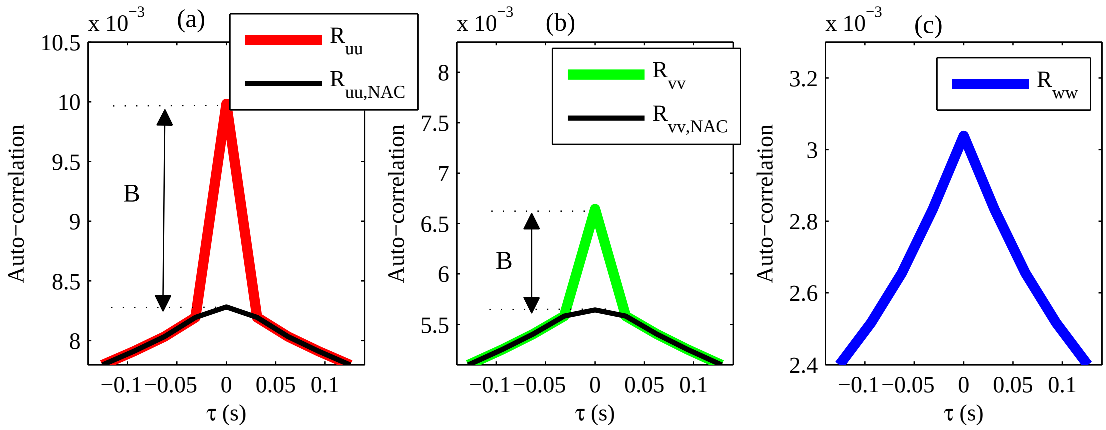

Figure 9: Section of auto-correlation plot highlighting ensemble-averaged auto-correlation close to zero τ for non-slack tidal condition, showing the spike in correlation due to contribution from instrument noise (i.e., B): (a) for the u component of velocity, R_{uu} and $R_{uu,NAC}$, (b) for the v component of velocity, R_{vv} and $R_{vv,NAC}$, and (c) for w component of velocity, R_{ww} without presence of spikes.

for u component of velocity, which are optimized for the velocity fluctuations, are shown in Fig. 13(a)-(f) (a similar result is obtained for v component of velocity, not shown). As observed from these figures, the modes have a definitive structure to them and they show an increase in number of peaks and valleys with increase in mode number, as well as a shift in the location of peaks and valleys. This suggests that the combination of modes may identify coherent structures present in the turbulent flow data and may also represent advection of coherent structures. The cumulative energy captured by the POD modes for u component of velocity is shown in Fig. 14. As observed in the figure, the higher order modes have captured significantly lower energy as compared to lower order POD modes. This suggests that the higher order POD modes may be associated with non-coherent structures or noise which is not energetic. A similar behavior is also observed for the v component of velocity (not shown here).

A low-order reconstruction is performed as shown in Fig. 13(g). As observed in the figure, a low-order reconstruction using first six POD modes is able to accurately capture the low frequency fluctuations. However, when the 359 POD modes which capture $\sim$ 80 percent of total energy (as can be seen from the Fig. 14) are used for the low-order reconstruction, the reconstructed velocity data almost exactly follow the original ADV data trend, while suppressing the high frequency fluctuations in the data.

In the following paragraphs, two versions of POD noise-correction, implemented for the u component of velocity, during non-slack tidal condition, are discussed in detail. These are implemented for v component of velocity as well (both non-slack and slack tidal conditions), however the implementation is not discussed in detail here because the results are similar.

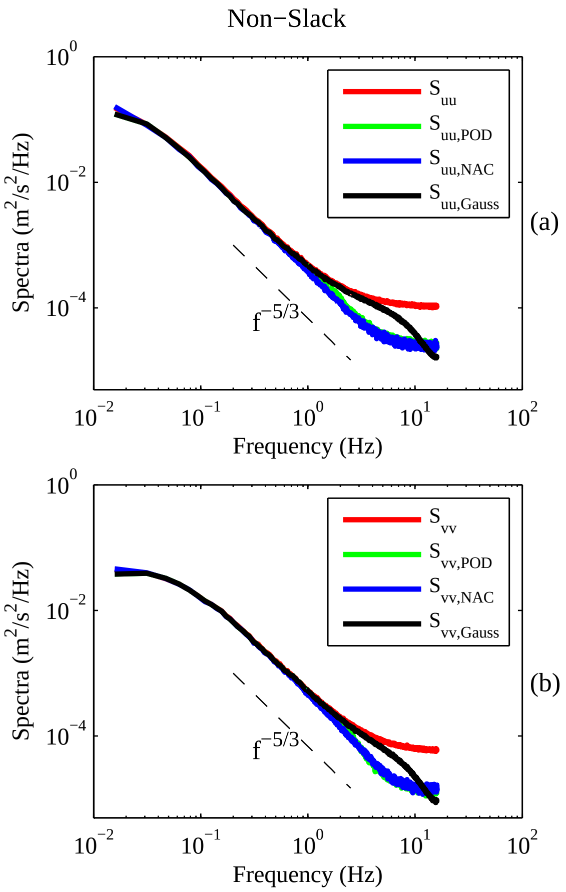

Figure 10: Ensemble-averaged spectra obtained from QC ADV data, NAC, POD and Gaussian filter approaches: (a) for u component of velocity during non-slack tidal condition, and (b) for v component of velocity during non-slack tidal condition.

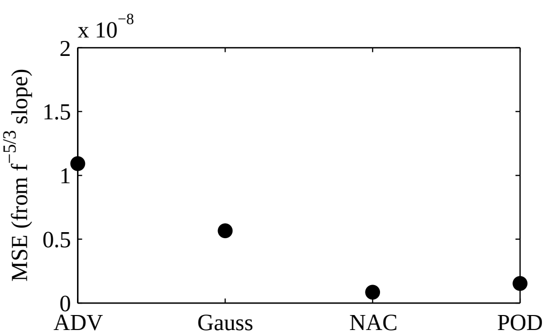

Figure 11: MSE of the spectra from the expected $f^{-5/3}$ slope for QC ADV data, Gaussian filter, NAC and POD approaches.

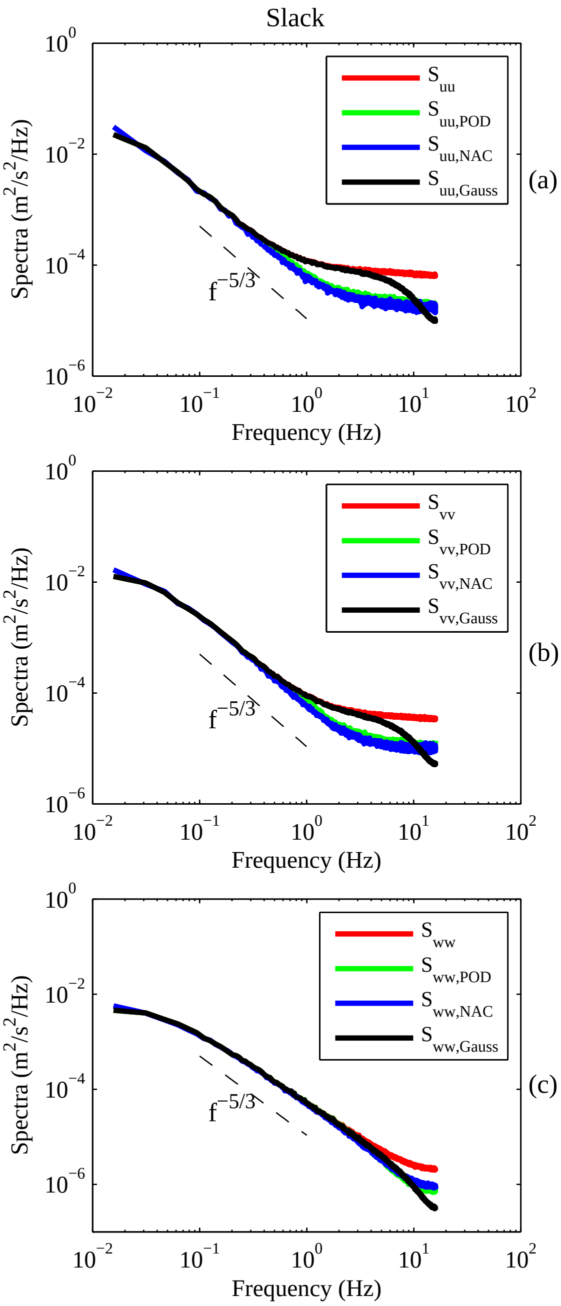

Figure 12: Ensemble-averaged spectra obtained from QC ADV data, NAC, POD and Gaussian filter approaches: (a) for u component of velocity during slack tidal condition, (b) for v component of velocity during slack tidal condition, and (c) for w component of velocity during slack tidal condition.

The first version assumes that the spectra for the energetic tidal flow follow a $f^{-5/3}$ slope in the inertial sub-range of the spectra. Several low-order reconstructions are calculated using Eq. 11, where N varies from 1 to 2048, which yield 3410 low-order-reconstructed velocity data records (i.e., total number of records in non-slack tidal condition) for each value of N. Spectra are then estimated from these low-order-reconstructed velocity data records for each value of N, and an ensemble-averaged spectrum is calculated from these spectra. Then, the Mean Square Error (MSE) of the ensemble-averaged spectrum from the expected $f^{-5/3}$ slope in the inertial sub-range (here, the frequency in the range of 1 Hz to 8 Hz) is calculated. The MSE as a function of mode number (N) used for the reconstruction is shown in Fig. 15. As observed in the figure, the MSE shows a significant variation with change in the mode number used for the low-order reconstruction. A physical explanation for the MSE is that initially, each additional mode captures additional information about coherent turbulence, but, above a certain number of POD modes (i.e., $N_{optimal}$), they are dominated by noise. The ensemble-averaged spectrum (i.e., $S_{uu,POD}$) calculated from these low-order reconstructions is shown in Fig. 10(a). As observed in the figure, low-order reconstruction using $N_{optimal} = 359$ modes is able to accurately capture the behavior of the spectra by attenuating instrument noise, and exhibits an $f^{-5/3}$ slope in the inertial sub-range.

The second version estimates the $N_{optimal}$ modes *a priori*, without assuming an $f^{-5/3}$ slope. In this approach, the λ's are related to the TKE (or variance $\langle u'^2 \rangle$) by

$$\langle u'^2 \rangle = \frac{1}{2048} \sum_{i=1}^{2048} \lambda i. \tag{15}$$

The variances for the u and v components of velocity for slack and non-slack tidal conditions are calculated directly from QC-ADV data and λs. The variances obtained from both these approaches have identical values. This suggests that the λs can be used to represent the total TKE from the ADV data. Now in a low-order reconstruction, if only a certain number of POD modes are used such that the cumulative TKE from the excluded POD modes is exactly equal to contribution from instrument noise i.e., B, this will yield ADV data with reduced instrument noise. The relationship between the cumulative TKE of the excluded modes (i.e., B) and $N_{optimal}$ can mathematically be defined as

$$\langle u'^2 \rangle - B = \frac{1}{2048} \sum_{i=1}^{N_{optimal}} \lambda i. \tag{16}$$

If the contribution from instrument noise i.e., B is known, the above equation can be used to estimate $N_{optimal}$. Using the B values from the NAC implementation results in $N_{optimal}$ values similar to the $N_{optimal}$ obtained by assuming an $f^{-5/3}$ slope. This self-consistency in the two versions of POD suggests an effective removal of noise, given *a priori* assumptions about either the noise or the true signal. Although POD requires significant assumptions, it has the advantage of retaining time domain information.

The ensemble-averaged spectrum (i.e., $S_{uu,POD}$) calculated from the low-order reconstructions using $N_{optimal}$ modes is shown in Fig. 10(a). There is an order of magnitude decrease in the noise floor level

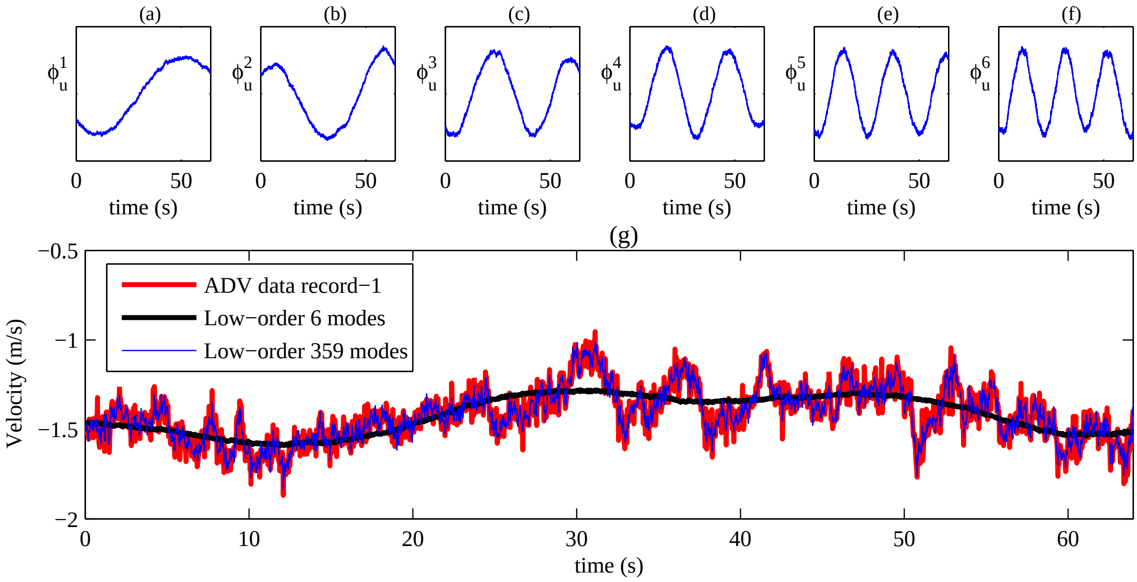

Figure 13: POD modes for non-slack tidal condition and low-order reconstruction: (a)-(f) first six POD modes for u component of velocity, and (g) u-component of velocity from ADV data record-1 along with low-order reconstruction using first 6 and 359 POD modes.

compared to the ensemble-averaged raw spectrum (i.e., S_{uu}). The POD spectrum extends the $f^{-5/3}$ inertial sub-range, and there is a decrease in the MSE error from the expected $f^{-5/3}$ slope (see Fig. 11).

A similar analysis for the v component of velocity (not presented here) shows that $N_{optimal} = 397$ POD modes. The ensemble-averaged spectrum for v component of velocity (for non-slack tidal condition) calculated from low-order reconstructions using 397 POD modes, is shown in Fig. 10(b), and exhibits a result similar to that of u component of velocity. The POD technique is also implemented for the slack tidal condition, and the resulting spectra for the slack tidal condition are shown in Fig. 12. These spectra exhibit a trend similar to that of the non-slack condition, suggesting that this approach can also be implemented in the case where turbulent flows are less energetic.

Even though the NAC and POD approaches are inherently different, they yield similar noise-corrected spectral results, corroborating the effective attenuation of instrument noise from QC ADV data. A separate comparison of the results for each of these approaches with theoretical isotropy follows in §4.4.

4.3. Gaussian filter implementation

The results obtained using the NAC and POD approaches are compared to results obtained using a conventional low-pass Gaussian filter, which is commonly used to remove high frequency noise [see 10, 21,

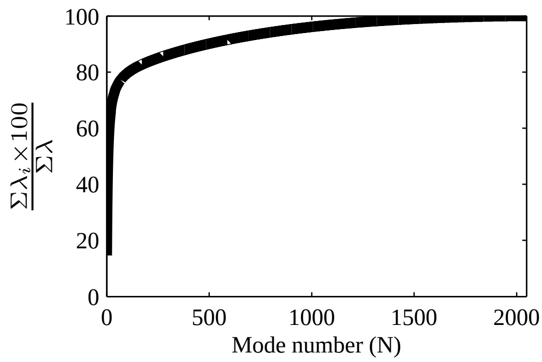

Figure 14: Cumulative energy in POD modes during non-slack tidal condition for u component of velocity.

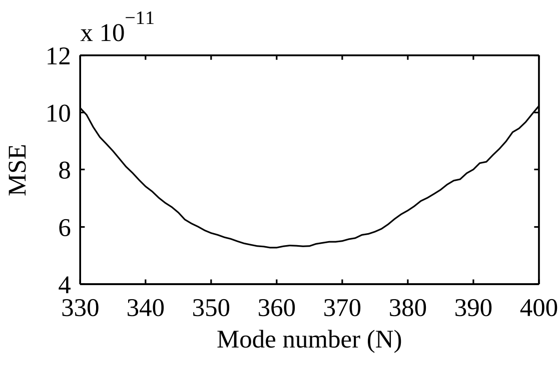

Figure 15: Mean Square Error (MSE) for u component of velocity for non-slack tidal condition as a function of the mode number (N) used for low-order reconstructions.

22, 23]. For this purpose, a filter with a smoothing function ($w(t)$) [20], given as

$$w(t) = \left(2\pi\sigma^2\right)^{-0.5} \exp^{-t^2/2\sigma^2}, \\ \sigma = \left(\frac{\ln(0.5)^{0.5}}{-2\pi f_{50}^2}\right)^{0.5}, \tag{17}$$

where, t is time, $f_{50} = f_D/6$, and f_D=32 Hz is the sampling frequency, is used. The QC ADV data are filtered and used to calculate the spectra for horizontal velocity components (i.e., $S_{uu,Gauss}$ and $S_{vv,Gauss}$) for non-slack tidal condition. The ensemble-averaged spectra obtained after filtering the QC ADV data are shown in Fig. 10. As observed in the figure, the instrument noise in the filtered data is eliminated at higher frequencies. However, spectra show a bump at a frequency of 8 Hz and shift away from the expected $f^{-5/3}$ slope in the inertial sub-range. Thus, although the Gaussian low-pass filter is capable of correcting for the instrument noise present at higher frequencies, it may not be able to do so at lower frequencies, resulting in a bump in the spectra and a deviation from the expected $f^{-5/3}$ slope. Figure 11 shows that there is a decrease in the MSE of the spectra from the expected $f^{-5/3}$ slope as compared to MSE of spectra obtained from QC ADV data, but the NAC and POD methods have significant reduction in MSE. A similar result is also observed for the slack tidal condition QC ADV data, as shown in Fig. 12.

4.4. Evaluation of isotropy

To evaluate the effectiveness of NAC and POD approaches in removing instrument noise from ADV data, the relationship between the horizontal and vertical spectra provided by Lumley and Terray [49] is utilized. The model spectra provided by Lumley and Terray [49] for a frozen inertial-range turbulence advecting past a fixed sensor is used to determine the ratio of spectra (R) for horizontal and vertical components. This quasi-isotropic ratio,

$$\mathrm{R} = \frac{(12/21)(S_{uu}(f) + S_{vv}(f))}{S_{ww}(f)}, \tag{18}$$

is predicted to be $\simeq 1.0$ in the inertial sub-range for the flow near the seabed (neglecting wave motions). See articles by Lumley and Terray [49], Trowbridge and Elgar [50], and Feddersen [18] for detailed derivation and analyses. Figure 16 shows the R values as a function of frequency, calculated from the QC ADV data, and noise removal approaches used in this study i.e., NAC, POD, and Gaussian filter techniques. As observed from the figure, the spectra obtained from QC ADV data and Gaussian low-pass filtered data acquire R values significantly higher than unity in the inertial sub-range of the spectra (i.e., for frequency higher than 2 Hz). However, for the NAC and POD techniques, R values stay close to unity for most of the inertial sub-range of the spectra (i.e., for frequencies from 1-8 Hz). The spectra obtained from NAC and POD approaches are consistent with the isotropic spectra suggested by [49]. In spite of the noise correction, at higher frequencies (i.e., frequencies higher that 8 Hz), R value deviates significantly from its theoretical unit value. This is because at these frequencies, the energy content of Doppler noise is significantly higher (even

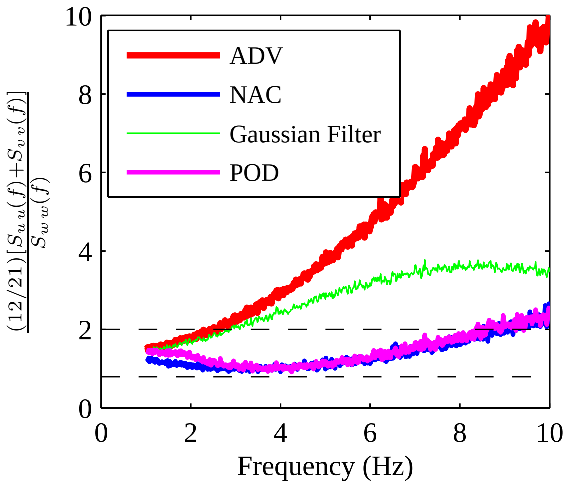

Figure 16: Variation of R as a function of frequency. The horizontal dashed line represents R values of 0.8 and 2.0.

after NAC or POD technique) compared to energy content of u and v components of velocity spectra. The w component of spectra will have significantly lower energy compared to the noise contaminated spectra of the horizontal velocity components at these frequencies. Therefore, the ratio of $S_{uu} + S_{vv}/S_{ww}$ will show a significant deviation from the expected result.

5. Application of NAC to improve estimates of the turbulent dissipation rate

One common use of ADV spectra is to estimate the dissipation rate of TKE. In this section, we apply the NAC method to the field data and demonstrate improved estimates of the dissipation rate, especially during less energetic (i.e., slack) tidal conditions. The improvement is primarily in the confidence (reduced uncertainty) of each dissipation estimate, however the NAC method also gives dissipation estimates more consistent with an expected local TKE budget. This application is restricted to the spectra of vertical velocity; other applications might benefit from applying the NAC method to horizontal velocities as well.

The dissipation rate ϵ is estimated from the ADV vertical velocity spectra $S_{ww}(f)$ shown in Fig. 12(c)

$$S_{ww}(f) = a\epsilon^{2/3} f^{-5/3}, \tag{19}$$

where f is frequency and a is the Kolmogorov constant taken to be 0.69 for the vertical component [51]. The vertical component is used because it has the lowest intrinsic Doppler noise (a result of ADV geometry). This approach utilizes Taylor's 'frozen field' hypothesis, which infers a wavenumber k spectrum as a frequency f spectrum advected past the ADV at a speed $\langle u \rangle$, such that $f = \langle u \rangle\, k$.

First, the raw spectra S_{ww} and NAC spectra $S_{ww,NAC}$ are calculated using five-minute bursts of the 32 Hz sampled ADV field data, which have stationary mean and variance over the burst. Next, an $f^{-5/3}$ slope is fit to the spectra in the range of $1 < f < 10$ Hz. The fitting is forced to $f^{-5/3}$ using MATLAB's *roubustfit* algorithm, and the intercept is set to zero. The standard error of the fit is retained and is propagated through Eq. 19 as a measure of the uncertainty σ_ϵ in the resulting ϵ values. The standard error is defined as the rms error between the fit and the spectra, normalized by the number of frequency bands used in the fitting.

The dissipation rates and uncertainties from all bursts are shown in Fig. 17 as a function of the burst mean horizontal tidal current $< u >$. The dissipation rates are elevated during strong tidal flows and are similar order of magnitude to estimates from other energetic tidal channels [33]. The dissipation rates from the raw spectra are consistently higher than the dissipation rates from the NAC spectra. The reduction in dissipation is expected owing to the reduction of velocity variance by the NAC method. The uncertainties in dissipation rates from the raw spectra also are consistently higher than the uncertainties from the NAC spectra. The reduction in uncertainties is a result of better fits, over a wider range of frequencies, to the $f^{-5/3}$ inertial sub-range. For either method, the 16 Hz maximum frequency is still expected to be well within the inertial sub-range, which should extend to $\mathcal{O}(10^2)$ Hz during slack conditions and $\mathcal{O}(10^4)$ Hz during strong tidal flows (see scaling discussion in §32.1).

The difference between methods is most pronounced during slack conditions ($\langle u \rangle < 0.8$ m/s), which is when Doppler noise is mostly likely to contaminate the ADV measurements (because the velocity signal is small compared with the noise). Under slack conditions, the uncertainties in raw dissipation rates are almost a factor of ten larger than the corresponding uncertainties in NAC dissipation rates. During more energetic tidal conditions, the vertical velocity spectra are elevated above the noise floor at most or all frequencies, and thus there is less disparity between the methods (although an overall bias is persistent).

Lacking independent measurements for validation of the dissipation results, a reasonable requirement is for the uncertainty of each dissipation rate to be small compared with the estimate itself (i.e., $\sigma_\epsilon \ll \epsilon$). For the raw estimates of dissipation, this condition is only met during strong tidal flows ($\langle u \rangle > 0.8$ m/s in Fig. 17). For the NAC estimates of dissipation, this condition is met during all except the weakest tidal flows ($\langle u \rangle > 0.1$ m/s in Fig. 17). Thus, the NAC method extends the range of conditions in which the turbulent dissipation rate can be estimated with high confidence.

Another approach to evaluate the dissipation results is to assess the TKE budget,

$$\frac{D}{Dt}(TKE) + \nabla \cdot \mathcal{T} = \mathcal{P} - \epsilon, \tag{20}$$

where $\frac{D}{Dt}$ is the material derivative (of the mean flow), $\mathcal{T}$ is the turbulent transport, $\mathcal{P}$ is production (via shear and buoyancy) and ϵ is dissipation rate (loss to heat and sound). In a well-developed turbulent boundary layer, a balance between production and dissipation is expected. Furthermore, in a well-mixed environment, the production term will be dominated by Reynolds stresses acting on the mean shear $\mathcal{P} = -\langle u'w' \rangle \frac{d\bar{U}}{dz}$, and buoyancy production can be neglected. (This assumption is corroborated by measurements

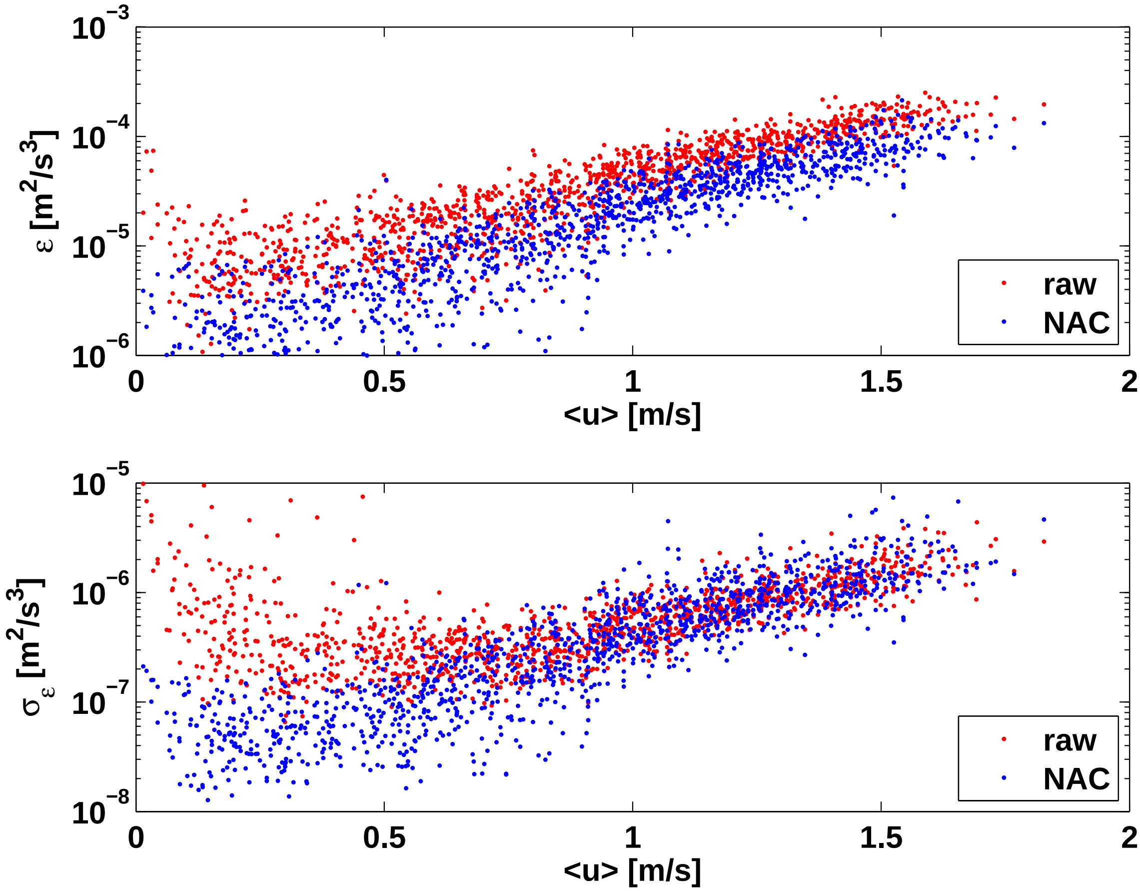

Figure 17: Dissipation rates (top) and uncertainties (bottom) versus mean horizontal speed obtained from raw spectra (red symbols) and NAC spectra (blue symbols).

of salinity stratification, using CTDs mounted at 1.85 and 2.55 m above the seabed on the ADV tripod, which showed < 0.05 PSU difference over all tidal conditions.) Here, Reynolds stresses are calculated directly from the ADV data, after rotation to principal axes, and the shear is calculated from collocated ADCP data with 0.5 m vertical resolution [see 30]. There is, of course, noise contamination in the estimation of Reynolds stresses $\langle u'w' \rangle$ from ADV, because u' and w' share noise from the same acoustic beams. However, this has a limited affect on the estimates because of the high frequency nature of the noise [9]. (This is in contrast to estimating the dissipation rate, which requires fidelity at high frequencies.)

The shear production and dissipation rates are compared in Fig. 18. The raw estimates of dissipation exceed shear production consistently. The NAC estimates of dissipation, by contrast, are scattered above and below the production. The rms error of an assumed $P - \epsilon$ balance during all tidal conditions is 4.7x10^{-5} for raw estimates and 1.6x10^{-5} for NAC estimates. As in the comparison of uncertainty, the difference in methods is most pronounced during less energetic conditions (i.e., $\epsilon < 10^{-5}$ in Fig. 18). The rms error of an assumed $P - \epsilon$ balance during slack tidal conditions is 2.0x10^{-5} for the raw estimates and 0.6x10^{-5} for the NAC estimates. Thus, results from the NAC method are more consistent, over a wider range of conditions, with the expected dynamics of a turbulent bottom boundary layer.

6. Conclusions

ADV measurements were collected from a proposed tidal energy site and used to evaluate two methods for noise-correction of velocity spectra. The raw spectra were flat at higher frequencies, consistent with previous studies on Doppler instrument noise. Both NAC and POD approaches were effective in decreasing the noise contamination of spectra, especially for high frequencies. The attenuation of instrument noise extends observations of the $f^{-5/3}$ inertial sub-range to more frequencies, and thus gives a better fit (i.e., more points) when estimating the dissipation rate. Moreover, a wider subrange obtained from these approaches may also be helpful in providing an accurate estimation of the dissipation rate when ADV data are further contaminated by waves and platform vibrations at select frequencies.

In comparison, the NAC and POD techniques show better agreement with an expected $f^{-5/3}$ slope than a conventional low-pass Gaussian filter approach. In the later approach, instrument noise is only removed above the cut-off frequency of the filter, and hence, the spectra may not be accurate just below the cut-off frequency.

The NAC approach provides a straightforward method for attenuating instrument noise in velocity spectra and does not require prior knowledge of the spectral shape. However, the NAC approach does not provide the noise-corrected data in the temporal domain as all the operations required for NAC approach are performed in the frequency domain. It should also be noted that the NAC approach is implemented on the assumption that the instrument noise has unlimited bandwidth, which needs to be investigated further. The

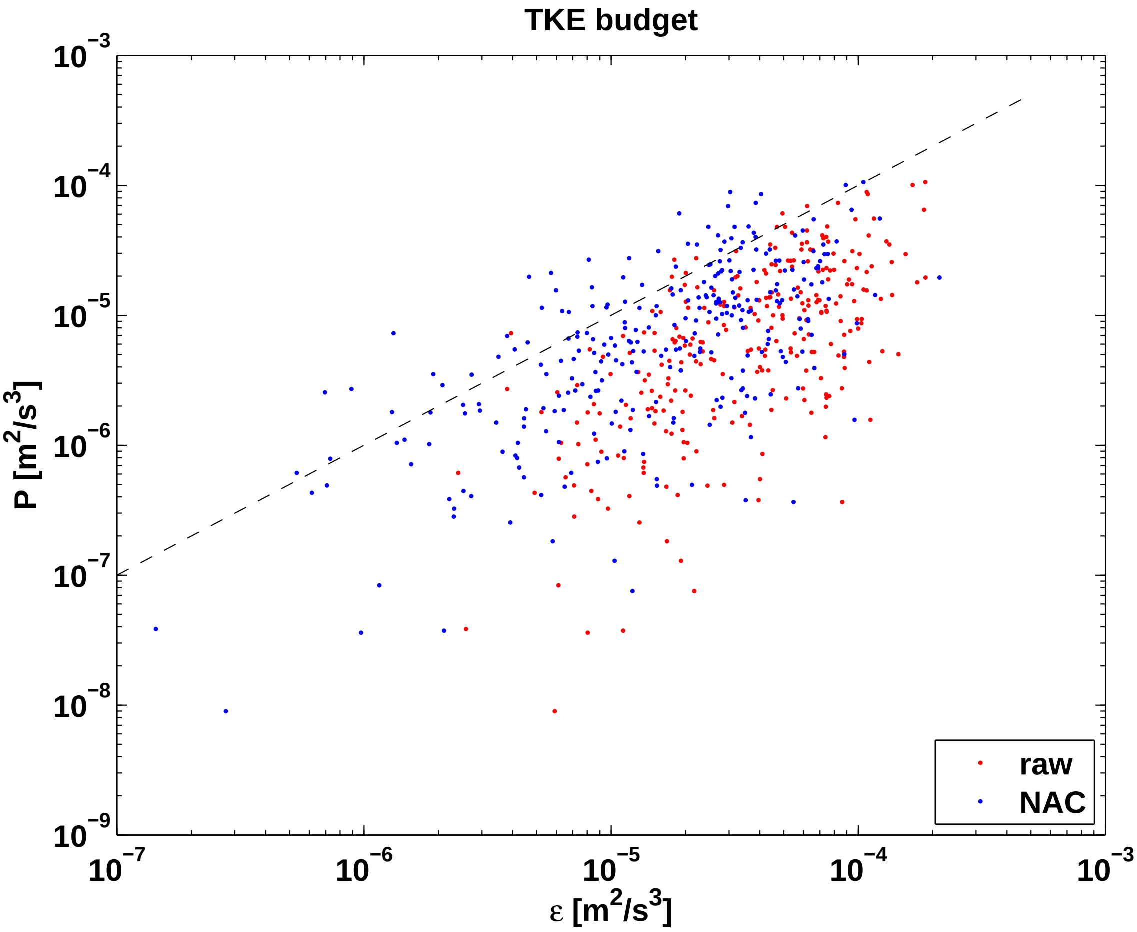

Figure 18: Shear production versus dissipation obtained from raw spectra (red symbols) and NAC spectra (blue symbols). All tidal conditions shown, processed in five-minute bursts. The dashed line indicates a 1:1 balance.

POD approach is capable of reducing instrument noise in spectra and in the temporal domain. However, the POD approach is more computationally intensive, requires prior knowledge of the noise level or spectral shape, and may not work in flows without dominant large scale coherent structures.

Acknowledgement

The Puget Sound field measurements were funded by the US Department of Energy, Energy Efficiency and Renewable Energy, Wind and Water Power Program. Thanks to Joe Talbert, Alex deKlerk, and Captain Andy Reay-Ellers of the University of Washington for help with field data collection.

[1] J. G. Venditti, S. J. Bennett, Spectral analysis of turbulent flow and suspended sediment transport over fixed dunes, Journal of Geophysical Research 105 (C9) (2000) 22035–22047.

[2] A. N. Sukhodolov, B. L. Rhoads, Field investigation of three-dimensional flow structure at stream confluences 2. turbulence, Water Resources Research 37 (9) (2001) 2411–2424.

[3] P. M. Biron, C. Robson, M. F. Lapointe, S. J. Gaskin, Three-dimensional flow dynamics around deflector, River Research and Application 21 (2005) 961–975.

[4] L. Ge, S. O. Lee, F. Sotirpoulos, T. Sturm, 3D unsteady RANS modeling of complex hydraulic engineering flows. ii: Model validation and flow physics, Journal of Hydraulic Engineering 131 (9) (2005) 809–820.

[5] J. Thomson, B. Polagye, M. Richmond, V. Durgesh, Quantifying turbulence for tidal power applications, Oceans-2010, MTS/IEEE, 2010.

[6] B. J. Jonkman, TurbSim user's guide: Version 1.50, National Renewable Energy Laboratory Colorado, 2009.

[7] S. Gant, T. Stallard, Modelling a tidal turbine in unsteady flow, in: Proceedings of the Eighteenth (2008) International Offshore and Polar Engineering Conference, The International Society of Offshore and Polar Engineers, 2008.

[8] V. I. Nikora, D. G. Goring, ADV measurements of turbulence: Can we improve their interpretation?, Journal of Hydraulic Engineering 124 (6) (1998) 630–634.

[9] G. Voulgaris, J. H. Trowbridge, Evaluation of Acoustic Doppler Velocimeter (ADV) for turbulence measurements, Journal of Atmospheric and Oceanic Technology 15 (1998) 272–289.

[10] C. M. Garcia, M. I. Cantero, Y. Nino, M. H. Garcia, Turbulence measurements with Acoustic Doppler Velocimeters, Journal of Hydraulic Engineering 131 (12) (2005) 1062–1073.

[11] A. N. Kolmogorov, The local structure of turbulence in incompressible viscous fluid for very large Reynolds numbers, Proceedings of the USSR Academy of Sciences 30 (1941) 299–303.

[12] S. B. Pope, Turbulent Flows, Cambridge University Press, 2000.

[13] S. A. Thorpe, An Introduction to Ocean Turbulence, Cambridge University Press, 2007.

[14] S. Elgar, B. Raubenheimer, Current meter performance in the surf zone, Journal of Atmospheric and Oceanic Technology 18 (2001) 1735–1745.

[15] T. L. Wahl, Discussion of despiking Acoustic Doppler Velocimeter data, Journal of Hydraulic Engineering 129 (6) (2003) 484–487.

[16] S. Elgar, B. Raubenheimer, R. T. Guza, Quality control of Acoustic Doppler Velocimetry data in the surfzone, Measurement Science Technology 16 (2005) 1889–1893.

[17] P. Mehran, S. Fotis, P.-A. Fernando, Estimation of power spectra of Acoustic-Doppler Velocimetry data contaminated with intermittent spikes, Journal of Hydraulic Engineering-ASCE 136 (6) (2010) 368–378.

[18] F. Feddersen, Quality controlling surfzone Acoustic Doppler Velocimeter observations to estimate the turbulent dissipation rate, Journal of Atmospheric Ocean Technical Volume 27 (12) (2010) 2039–2055.

[19] D. G. Goring, V. I. Nikora, Despiking Acoustic Doppler Velocimeter data, Journal of Hydraulic engineering (2002) 117–126.

[20] S. N. Lane, P. M. Biron, K. F. Bradbrook, J. B. Butler, J. H. Chandler, M. D. Crowell, S. J. Mclelland, Three-dimensional measurement of river channel flow processes using Acoustic Doppler Velocimetry, Earth Surface Processes and Landforms 23 (1998) 1247–1267.

[21] L. Cea, J. Puertas, L. Pena, Velocity measurements on highly turbulent free surface flow using ADV, Experiments in Fluids 42 (2007) 333–348.

[22] P. E. Carbonneau, N. E. Bergeron, The effect of bedload transport on mean and turbulent flow properties, Geomorphology 35 (3-4) (2000) 267 – 278.

[23] K. B. Strom, A. N. Papanicolaou, ADV measurements around a cluster microform in a shallow mountain stream, Journal of Hydraulic Engineering 133 (12) (2007) 1379–1389.

[24] D. Hurther, U. Lemmin, A correction method for turbulence measurements with a 3d Acoustic Doppler Velocity Profiler, Journal of Oceanic Engineering 18 (2001) 446–458.

[25] J. L. Lumley, The stucture of inhomogeneous turbulence, in: A. M. Yalglom, V. I. Tatarski (Eds.), Atmospheric Turbulence and Radio Wave Propogation, Nauka, Moscow, 1967, pp. 166–178.

[26] P. Holmes, J. L. Lumley, G. Berkooz, Turbulence, Coherent Structures, Dynamical Systems and Symmetry, 1st Edition, Cambridge University Press, 1996.

[27] M. N. Glauser, W. K. George, Orthogonal decomposition of the axisymmetric jet mixing layer including azimuthal dependence, Advances in Turbulence: Proceeding of the European Turbulence Conference (1987) 357–366.

[28] J. H. Citriniti, W. K. George, Reconstruction of the global velocity field in the axisymmetric mixing layer utilizing the Proper Orthogonal Decomposition, Journal of Fluid Mechanics 418 (2000) 137–166.

[29] J. P. Bonnet, J. Lewalle, M. N. Glauser, Coherent structures, past, present, and future, in: Advances in Turbulence, Prceedings of the European Turbulence Conference, Vol. 6, 1996, pp. 83–90.

[30] J. Thomson, B. Polagye, V. Durgesh, M. Richmond, Measurements of turbulence at two tidal energy sites in Puget Sound, WA (USA), Journal of Oceanic Engineering 37 (2012) 363–374.

[31] M. Palodichuk, B. Polagye, J. Thomson, Resource mapping at tidal energy sites, Journal of Oceanic Engineering (2013) Accepted for publication.

[32] M. T. Stacey, S. G. . Monismitha, J. R. Burau, Measurements of Reynolds stress profiles in unstratified tidal flow, Journal Of Geophysical Research 104 (C5) (1999) 10933–10949.

[33] P. J. Wiles, T. P. Rippeth, J. H. Simpson, , P. J. Hendricks, A novel technique for measuring the rate of turbulent dissipation in the marine environment, Geophysical Research Letter 33 (L21608).

[34] W. J. Emery, R. E. Thomson, Data Analysis Methods in Physical Oceanography, second and revised edition Edition, Elsevier, 2004.

[35] A. Lohrmann, R. Cabrera, N. C. Kraus, Acoustic Doppler Velocimeter (adv) for laboratory use, Proc. Symp. on Fundamentals and Advancements in Hydraulic Measurements and Experimentation (1994) 351–365.

[36] R. K. Walter, N. J. Nidzieko, S. G. Monismith, Similarity scaling of turbulence spectra and cospectra in a shallow tidal flow, Journal Of Geophysical Research in press.

[37] A. Papoulis, S. U. Pillai, Probability Random Variables and Stochastic Processes, 4th Edition, McGraw-Hill, 2002.

[38] J. S. Bendat, A. G. Piersol, Random Data Analysis and Measurement Procedures, 4th Edition, Wiley, 2010.

[39] H. Kantz, T. Schreiber, Nonlinear Time Series Analysis, 2nd Edition, Cambridge, 2004.

[40] J. Delville, L. Ukeiley, L. Cordier, J. P. Bonnet, M. Glauser, Examination of large-scale structures in a turbulent plane mixing layer. part-1- Proper Orthogonal Decomposition, Journal of Fluid Mechanics 391 (1999) 91–122.

[41] P. B. V. Johansson, W. K. George, Far downstream evolution of the high reynolds number axisymmetric wake behind a disk, part 1: Single point statistics, Journal of Fluid Mechanics 555 (2006) 363–385.

[42] V. Durgesh, R. Semaan, J. Naughton, Revealing unsteady flow structure from flow visualization images, The European Physical Journal - Special Topics 182 (2010) 35–50.

[43] L. Carassale, M. M. Brunenghi, Statistical analysis of wind-induced pressure fields: A methodological perspective, Journal of Wind Engineering and Industrial Aerodynamics 99 (6-7) (2011) 700 – 710.

[44] L. Sirovich, Turbulence and the dynamics of coherent structures part-1: Coherent structures, Quarterly of Applied Mathematics 45 (3) (1987) 561–571.

[45] L. Sirovich, Turbulence and the dynamics of coherent structures part-2: Symmetries and transformations, Quarterly of Applied Mathematics 45 (3) (1987) 573–582.

[46] L. Sirovich, Turbulence and the dynamics of coherent structures part-3: Dynamics and scaling, Quarterly of Applied Mathematics 45 (3) (1987) 583–590.

[47] M. Ghil, M. Allen, M. Dettinger, K. Ide, D. Kondrashov, M. Mann, A. Robertson, A. Saunders, Y. Tian, F. Varadi, P. Yiou, Advanced spectral methods for climatic time series, Rev. Geophys. (USA) 40 (1).

[48] M. Romagnoli, C. M. Garcia, R. A. Lopardo, Signal postprocessing technique and uncertainty analysis of ADV turbulence measurements on free hydraulic jumps, Journal of Hydraulic Engineering 138 (4).

[49] J. L. Lumley, E. A. Terray, Kinematics of turbulence convected by a random field, Journal of Physical Oceanography 13 (1983) 2000–2007.

[50] J. Trowbridge, S. Elgar, Turbulence measurements in the surf zone, Journal of Physical Oceanography 31 (8) (2001) 2403–2417.

[51] K. R. Stapleton, D. A. Huntley, Seabed stress determinations using the inertial dissipation method and the turbulent kinetic energy method, Earth Surface Processes and Landforms 20 (9) (1995) 807–815.